Article

Preparation of UV-Curable Nano-WO$_3$Coating and Its Infrared Shielding Properties

Zhengjie Wang, Rong Zhong *, Ting Lai and Tianlei Chen

School of Environmental and Chemical Engineering, Nanchang Hangkong University, Nanchang 330063, China
* Correspondence: zhongr@nchu.edu.cn

Abstract: Nano-WO$_3$ particles are expected to find use in new shielding materials because of their significant absorption of near-infrared light in the 1400–1600 nm and 1900–2200 nm bands and high transmittance of visible light. In this study, WO$_3$ was ground and dispersed using high-energy ball-milling to prepare a nano-WO$_3$ dispersion using BYK331 as the dispersant and ethanol as the solvent. The prepared nano-WO$_3$ dispersion was added to a photo-curing system and cured using UV irradiation to form films. The cured films were characterized using FT-IR, SEM, XRD, and TGA. The results showed that the nano-WO$_3$ powder was evenly dispersed in the coating. The infrared blocking rate of the film continuously improved and the visible light transmission rate continuously decreased with increasing amounts of nano-WO$_3$.For the film containing 6 wt%nano-WO$_3$, the infrared blocking rate of the coating is 90%, the visible light transmittance is 70%, the hardness of the coating is 3B, and the adhesion is 3H. The thermal stability of the coating is also improved.

Keywords: nano-tungsten oxide; IR shielding coating; UV-curable; high-energy ball-milling

1. Introduction

Glass materials are used widely in the construction, electronic, automobile, and aeronautic industries [1]. Traditional window glass is usually composed of soda lime glass [2], which is made of silica, calcium oxide, sodium oxide, and a small amount of other additives through a float process [3–5]. The transmittance of transparent soda lime glass for near-infrared light at 4mm thickness is approximately 75–90% [6]. Near-infrared light (700–3000 nm) is the spectral region with the highest thermal energy [7], accounting for approximately52% of the total solar energy received on surfaces [8]. The high transmittance of glass for near-infrared light can easily cause temperature rise in internal spaces and produce light pollution [9–12]. Thus, materials for near-infrared light shielding have attracted the attention of many researchers and engineers.

At present, the most common infrared shielding materials are indium tin oxide (ITO) and antimony tin oxide (ATO), which can effectively block the near-infrared spectrum [13–16]. Khan et al. [17] prepared a multilayer nano-MgF$_2$/ITO coating via electron beam evaporation. The composite coating has good infrared shielding ability, and its visible light transmittance can reach 90%. Wang et al. [18] prepared hollow ATO microspheres via a hydrothermal method with carbon spheres as templates. The ATO hollow microspheres have high specific heat capacity, high infrared emissivity, and low thermal conductivity, and effectively enhanced the photo thermal shielding performance of silicone acrylic lotion coating. However, the raw materials ITO and ATO can only shield wavelengths greater than 1500 nm [19,20], which limits their large-scale commercial applications. Some noble metal nanoparticles can also shield infrared light [21–23], but their utility in infrared shielding materials is limited by their low transmittance of visible light. Limited rare earth compounds, such as LaB$_6$, PrB$_6$, and NdB$_6$ [24–27], can also effectively shield infrared light. However, they are expensive and large amounts of energy are required to crush their hard surfaces, making themun suitable for large-scale commercial production.The infrared shielding

ability of cesium tungsten bronze is better than that of ITO and ATO, and it thus shows great application prospects in infrared shielding materials [28–30].Song et al. [31] prepared K-and C_S-Co doped tungsten bronze ($K_m Cs_n WO_3$, m + n = 0.32) via a solid-state reaction method. Their results showed that K-and C_S-Co doping can promote the formation of W^{5+}, enhance local surface plasm on resonance (LSPR), and improve near-infrared shielding performance at 730–1100 nm. The visible light transmittance of the materials reached66.89% and their near-infrared shielding rate reached 98.25%. Zhang et al. [32] prepared Li-C_S-Co doped tungsten bronze nanoparticles with excellent near-infrared shielding properties via a simple solid-state reaction method. The results showed that Li^+ doping can control the growth of $Cs_x WO_3$ crystals to form hexagonal nanorods with high aspect ratio and improve the near-infrared shielding performance. Tungsten-oxide-based materials have attracted attention because of their superior near-infrared shielding performance. However, there have been few reports of the direct dispersion of nano-WO_3 into UV-cured coatings to achieve efficient infrared light shielding.

Nano-WO_3 particles have small particle size, insufficient atomic coordination, large specific surface area, and high surface energy, which can cause the nanoparticles to exhibit high activity, instability, and easy agglomeration [33,34]. Appropriate physical or chemical methods [35–37] must be adopted to modify the nanoparticles to obtain nanoparticles with good dispersion, small particle size, and narrow particle size distribution. High-energy ball-milling is a new surface modification method that can significantly reduce reaction activation energy, achieve grain refinement, greatly improve the activity of powder, and improve particle size distribution uniformity, and enhanced with the combination of the interface between the body, and thus improve the compactness of the material, along with its electrical and thermal performance. This method is an energy-saving and efficient material preparation technology.

In this study, nano-WO_3 is uniformly dispersed in a solvent using high-energy ball-milling. By changing the grinding and dispersion time, the dispersant, the proportions of the powder and dispersant, and the solvent, and examining the influence of these parameters on the dispersion system, a dispersive preparation process is developed. The obtained nano-WO_3 dispersion is added to an UV-curable coating to prepare a nano-WO_3-PUA composite coating. The aim of this study was to obtain an infrared shielding material for application to the surface of glass.

2. Experimental Section

### 2.1. Materials and Instruments

Nano WO_3 (99.99%) was purchased from Aladdin Chemical Co., Ltd., Shanghai, China. BYK331 (50 wt%) was purchased from BYK additives Co., Ltd., Wesel, Germany.Ethyl acetate, ethanol, and n-butyl acetate were purchased from Guangzhou Xinguan Chemical Co., Ltd., Guangzhou, China. Polyurethane acrylate (B-619w) was purchased from Guangzhou BOXING Chemical Co., Ltd., Ghuangzhou, China. Monomer (HDDA) was purchased from Taiwan Changxing Chemical Co., Ltd., Guangzhou, China. The photoinitiator (184) was purchased from Tianjin JIURI New Materials Co., Ltd., Tianjin, China.

2.2. Preparation of Nano-WO_3Dispersion

The desired amounts of dispersant and solvent were added to the mixer, and the stirring speed was set to 2500 rpm.After 30 min of stirring, nano-WO_3 powder was added, and stirring was continued for an additional 30 min. The stirred dispersion was placed into the ball-milling apparatus and ground using 0.8 mm zirconium beads at a grinding speed of 3800 rpm for a grinding time of 4 h.Subsequently, 0.1 mm zirconium beads were used at a grinding speed of 3800 rpm for a grinding time of 4 h. Samples were taken every hour and a nanoparticle size meter was used for particle size measurement.

2.3. Preparation of Light Curing Coatings

The preparation of light curing coatings is shown in Scheme 1. A formula containing the resin, monomer, and photoinitiator was used as the organic component of the UV-curable system. The proportion of B-619w was approximately 80% (*w/w*), the proportion of HDDA was 15%, the proportion of 184 was 5%. To this, 2wt%, 4wt%, 6wt%, and 8wt% nano-WO_3 was added, respectively, and the mixture was diluted to 50% solid content with ethanol. The mixture was coated onto the glass with a 20# wire rod, baked in an oven at 80 °C for 1min, and then plated into a curing machine for curing.
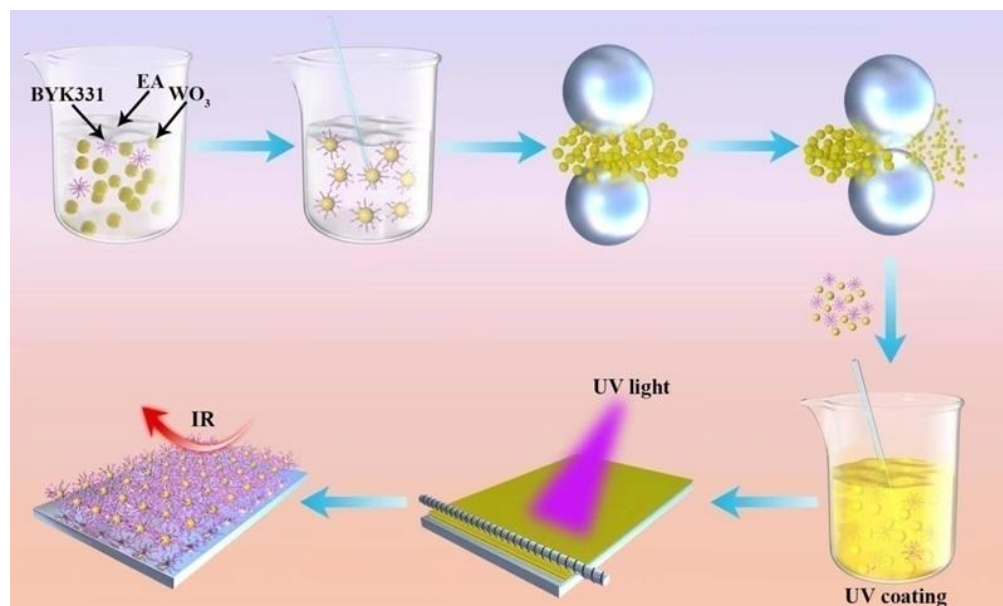
Scheme 1. Preparation of UV-curable nano-WO_3 coating.

2.4. Characterization

2.4.1. Particle Size Analysis

The desired amount of the nanodispersion was placed in a beaker and diluted 20–30 times with toluene, stirred to uniformity. The diluted dispersion was taken up with a pipette and added to the cuvette, which was then placed into the particle size analyzer. The particle sizes were measured. Each sample was measured in three groups with ten measurements in each group.

2.4.2. Infrared Spectrum Analysis

The cured film was peeled off from the substrate and ground into powder. Samples were prepared using the KBr tablet method and measured using a Nicolet Magna380 infrared spectrometer. The absorption peaks appearing at different positions were used to analyze the structure and composition of the substance.

2.4.3. Field Emission Scanning Electron Microscope (SEM)

A small amount of the sample was evenly coated on the silicon wafer using a rubber dropper, dried, and solidified into a film. The sample was placed in a Nova SEM 450 field emission scanning electron microscope for scanning.

2.4.4. X-ray Diffraction (XRD)

The coatings were characterized using a D8 advance X-ray powder diffractometer from Bruker, Germany. A portion of the sample was scraped from the cured coating and ground. A small amount of ground solid powder was placed in the instrument for scanning, The working voltage was set to 40 kV, the working current to 40 mA, the scanning angle to be 10–80°, and the scanning speed to be 3°/min.

2.4.5. Thermogravimetric Analysis (TGA)

A small amount of film was scraped off the surface of the cured layer with a blade and then characterized using a Perkin-Elmer Diamond TG/DTA thermal analyzer in an argon atmosphere from 25 °C to 800 °C at a heating rate of 10 °C/min.

2.4.6. Haze Analysis

The cured films were placed in a haze tester to test their haze. Haze measurements were taken at three positions, and the average value was taken as the haze of the layer.

2.4.7. Absorbance Analysis

The cured coating film was placed horizontally in an LS160 transmittance meter. Upper, middle, and lower positions of the coating were measured, and the IR blocking rate and visible light transmission rate of the coating were recorded. Finally, the average value of the upper, middle, and lower positions was taken as the transmittance of light at different wavelengths for the layer.

3. Results and Discussion

3.1. Effect of Grinding Time on Particle Size of Nano-WO₃

It can be seen from Figure 1a that when 0.8mm zirconium beads are used for grinding, due to the large particle size of the grinding medium, the kinetic energy of the grinding medium is relatively large at a specific grinding speed, and the grinding effect of nanoparticles is relatively good. Therefore, the particle size of nano-WO$_3$ decreases rapidly. However, when the grinding time exceeds 4h, the effective collision between the WO$_3$ particles and the grinding medium is reduced due to the large gap between the grinding media and the small particle size of the nano-WO$_3$, so the particle size of the nano-tungsten oxide no longer decreases. With continued grinding, the internal temperature of the system continues to rise, the solvent is volatilized, the viscosity of the system increases, the nanoparticles cannot be effectively dispersed, and agglomeration occurs again, and the particle size tends to increase, which may cause the system to become gelatinous and cause grinding failure.
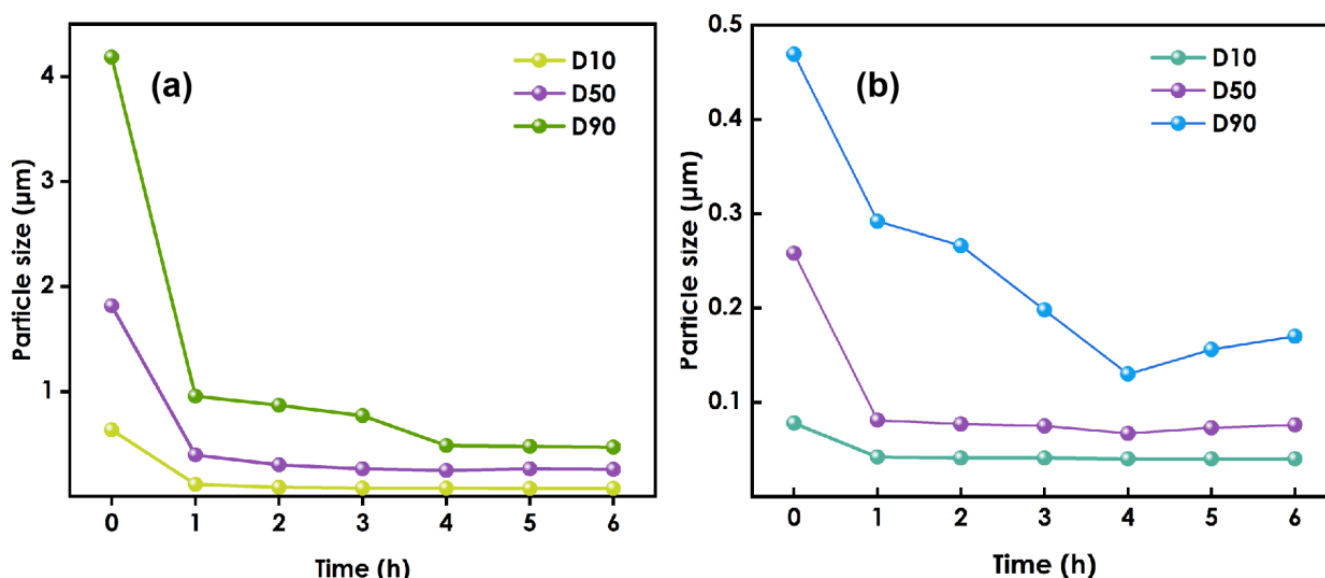

Figure 1. The figure of particle size variation:(**a**) used 0.8 mm zirconium beads, (**b**) used 0.1 mm zirconium beads.

After grinding had been performed using 0.8 mm zirconium beads for 4 h, the 0.1 mm zirconium beads were replaced and grinding was continued(Figure 1b). Due to the reduction in the size of the grinding medium, the number of beads will increase for a given

amount of medium. The gaps between the beads will be reduced, so the grinding and dispersion of nano-WO_3 will be more thorough, and the particle size of nano-WO_3 will continue to decrease. However, when grinding was performed for more than 4 h using the 0.1 mm zirconium beads, the particle size increased.

Therefore, during the experiment, the slurry was sampled every hour to test the slurry particle size, and when the decreasing trend in the size slows or it begins to increase, the initial grinding medium should be replaced with smaller beads to make the grinding more efficient.

3.2. Effects of the Amount of Dispersant

Figure 2 shows the change in the particle size for nano-WO_3 to dispersant ratios of 1:1, 1:2, and 2:1. During the first two hours of the grinding process, the average nano-WO_3 particle sizes of the three groups are similar. However, beyond two hours the reduction in the nano-WO_3 particle size for the WO_3:BYK331 = 2:1 group is slower than that of the WO_3: BYK331 = 1:1 group, and the final average particle size for the 2:1 group is larger. This is because, as the grinding progresses, the size of the nanoparticles continues to decrease, and the specific surface area of the particles continues to increase. When the amount of dispersant is small, it is difficult for the organic groups of the dispersant to completely coat the nano-WO_3 particles. The tendency of the particles to agglomerate due to intermolecular covalent bonds or the van der Waals force becomes larger, and their dispersion becomes more difficult. For the WO_3:BYK331 = 1:2 group, due to the high-speed rotation of the grinding medium during the grinding process, a large amount of heat is generated, resulting in a sharp rise in the internal temperature of the grinding system. The failure of the condensation system to immediately cool down will lead to a large amount of volatilization of organic solvents in the system. Moreover, the effective components in the dispersant will gelatinize, resulting in an increase in the viscosity of the system. The whole slurry will become colloidal, making it difficult to disperse. As shown in the figure, when nano-WO_3:BYK331=1:1, the system is relatively stable and the grinding effect is the best.
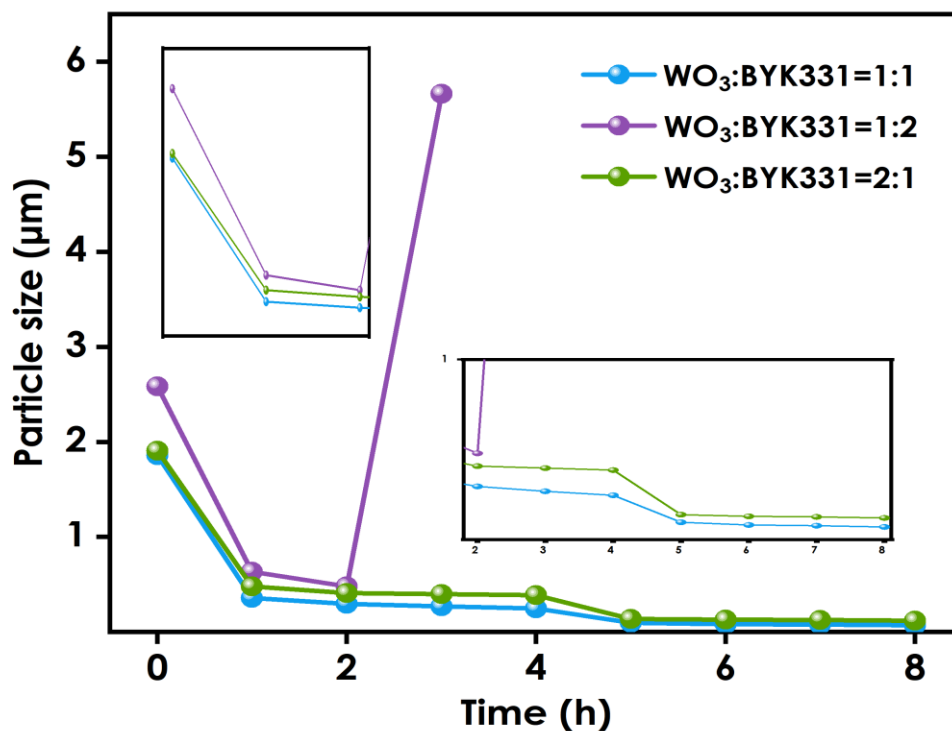

Figure 2. Particle size variation using different nano-WO_3:dispersant ratios.

3.3. Effects of Solvent on the Dispersion of Nano-WO$_3$

To explore the influence of different solvents on the dispersion of nano-WO$_3$, experiments using ethyl ester, ethanol, and butyl ester were conducted. The samples were ground using 0.8 mm zirconium beads for 4 h, and there after with 0.1 mm zirconium beads for an additional 4 h, after which their particle sizes were tested. As shown in Figure 3, the particle sizes in the dispersion systems using different solvents were similar throughout the different stages of the grinding process, and the final particle size difference after grinding was less than 10nm. Therefore, it can be concluded that the choice of solvent has little effect on the dispersion effect of nano-WO$_3$.
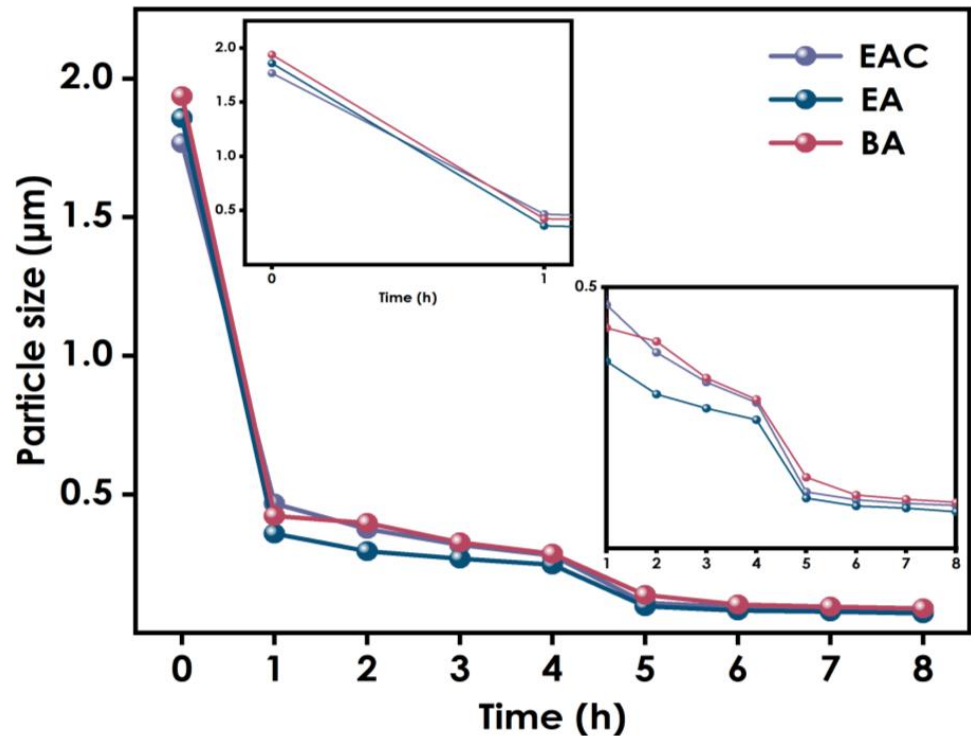

Figure 3. Particle size variation using different solvents.

3.4. Particle Size Distribution of Nano-WO$_3$Dispersion

The results of the above experiments indicate that the optimal conditions for the WO$_3$ dispersion process are ethanol as the solvent in a proportion of 50%, nano-WO$_3$ is 25%, and the BYK331proportion of 25%. The sample was ground with 0.8mm zirconium beads for 4 h and thereafter ground with 0.1 mm zirconium beads for a further 4 h at a grinding speed of 3800 n/min. The particle size diagram of nano-WO$_3$ after grinding and dispersion is shown in Figure 4. After grinding and dispersion of the nano-WO$_3$, the D50 is 54 nm and the D90 is 73 nm, the particle size distribution is narrow and the particle size is uniform.

3.5. FT-IR Testing of Composite Coatings

The FT-IR spectra of coatings prepared using different amounts of nano-WO$_3$ (0%, 2 wt%, 4wt%, 6 wt%, and 8 wt%) are shown in Figure 5. The stretching vibration of O-W-O is the peak at 810 cm^{-1}. The peak at 750 cm^{-1} is the characteristic absorption peak of W-O. The peak at 3375 cm^{-1} may be the characteristic absorption of W-O-H. The spectra exhibit the characteristic vibration peak of C=O at 1725 cm^{-1} for polyurethane methyacrylate. The absorption peak at 2931 cm^{-1} may be the characteristic absorption peak of -CH$_2$ in the system. With increasing WO$_3$ content, the intensity of the absorption peaks increased. These proved that WO$_3$was successfully introduced into the coatings.
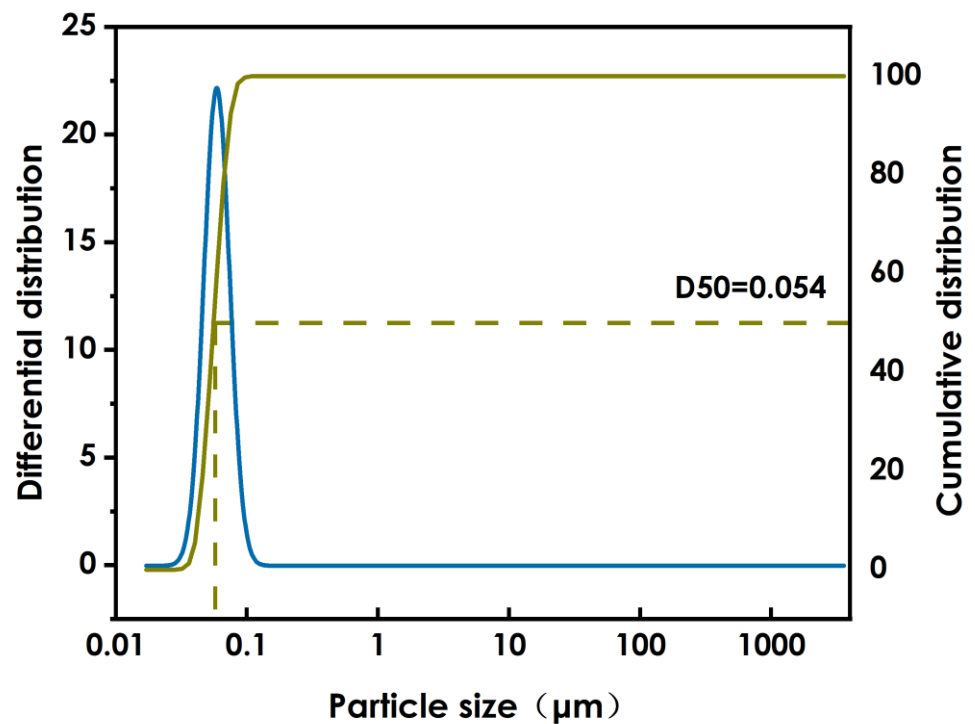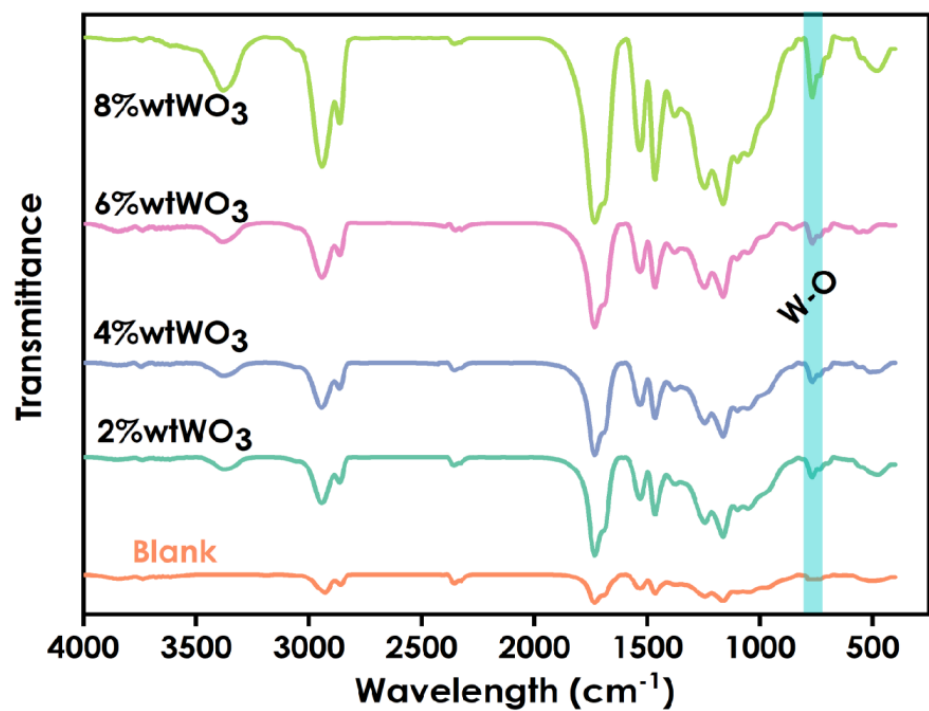
Figure 4. WO_3 particle size.

Figure 5. Infrared spectra of coatings prepared using different amounts WO_3(0%,2%,4%,6%,8%).

3.6. Morphology Analysis of Composite Coatings

Figure 6a presents the morphology of the coating prepared using unmodified WO_3 and Figure 6b presents the morphology of a coating prepared using milled WO_3. The figure shows that when nano-WO_3 is introduced into the UV-curing coating, serious agglomeration occurs, while the milled nano-WO_3 is evenly dispersed in the coating

without obvious agglomeration. The sizes of the nano-WO_3 are approximately between 20–200 nm.
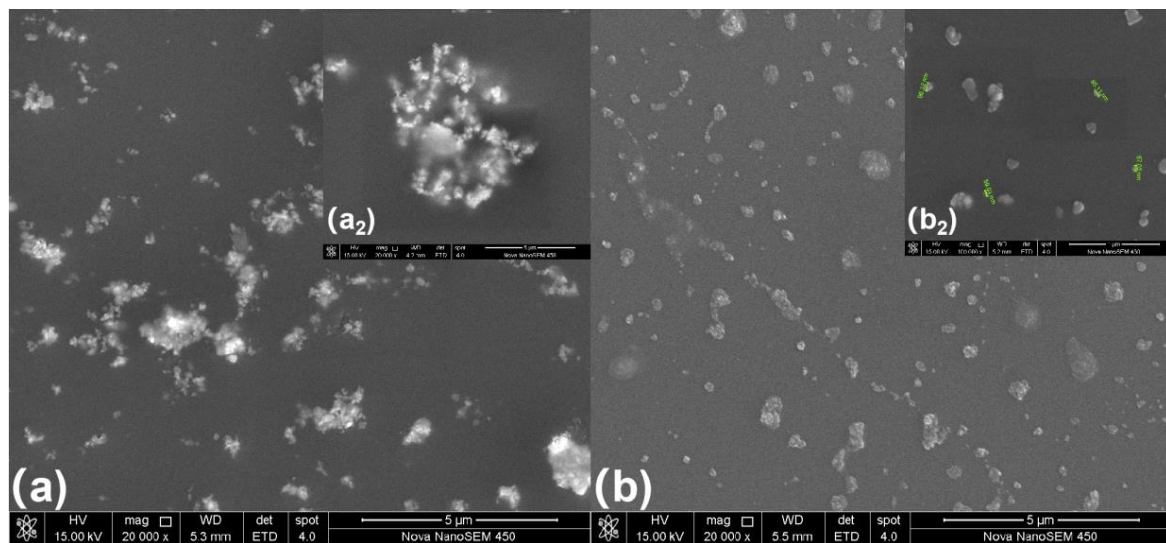

Figure 6. Morphology of composite coating: (**a**) the coating using unmodified WO_3, (**b**) coating using milled WO_3.

3.7. XRD Analysis of Composite Coating

The XRD patterns of the coatings prepared using different amounts of WO_3 dispersions(0, 2%, 4%, 6%, and 8%) are shown in Figure 7. The spectra of the WO_3-containing coatings show two sharp absorption peaks at 2θ of 23.43°and 24.38° that are not observed for the coating without WO_3, and with increasingWO_3addition the intensities of these diffraction peaks and their peak areas increase. A weak diffuse reflection is observed at 33.72°, and it becomes sharper with the addition of more WO_3. These indicate that the WO_3 phase is present in the layer, and that as the amount of added WO_3increases, the crystallinity of the crystalline phase becomes higher.
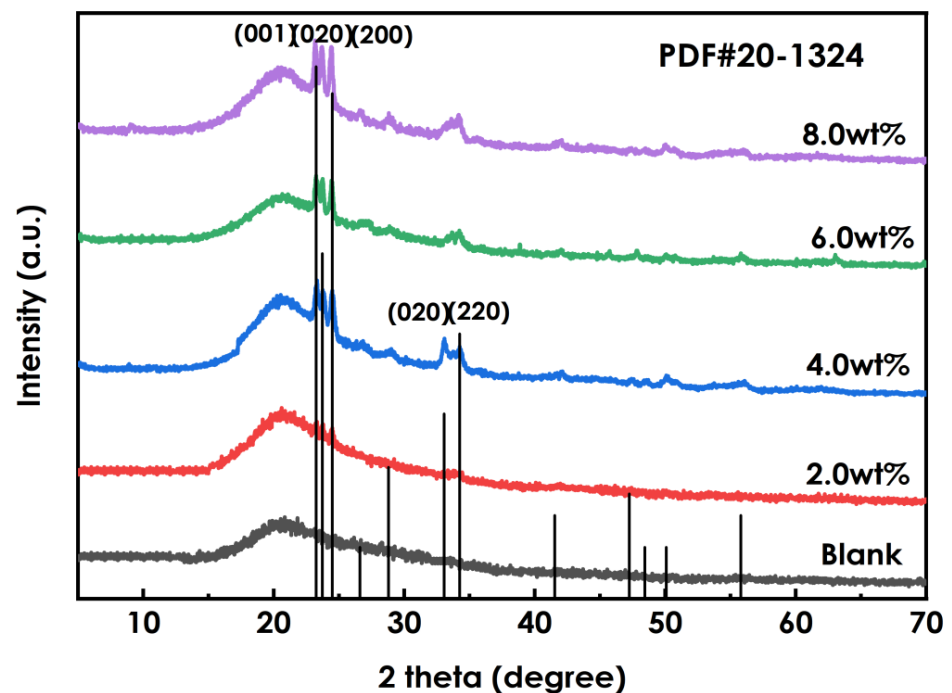

Figure 7. XRD patterns of coating using different amounts of WO_3.

3.8. Thermal Stability Analysis of Composite Coatings

Figure 8 presents the TG data for the coatings prepared using different amounts of WO₃, and Figure 9 presents the DTG data. As shown in Figure 8, he decomposition process of the coating at 0~800 °C can be roughly divided into two stages: 60–98 °C and 98–344 °C. Figure 9 shows that the maximum weight loss peak of the coating occurs at approximately 400 °C. The weight loss in the first stage is mainly due to the volatilization of residual solvent and free water in the system, and the weight loss rate is approximately 2%. The weight loss in the second stage is due to the decomposition of organic matter in the photo-curing system such as resin and monomer. The 6% WO₃coating shows the best thermal stability. Overall, the decomposition process of coatings prepared using different amounts of WO₃ is roughly the same, and the addition of WO₃ has little effect on the thermal stability of the coatings.
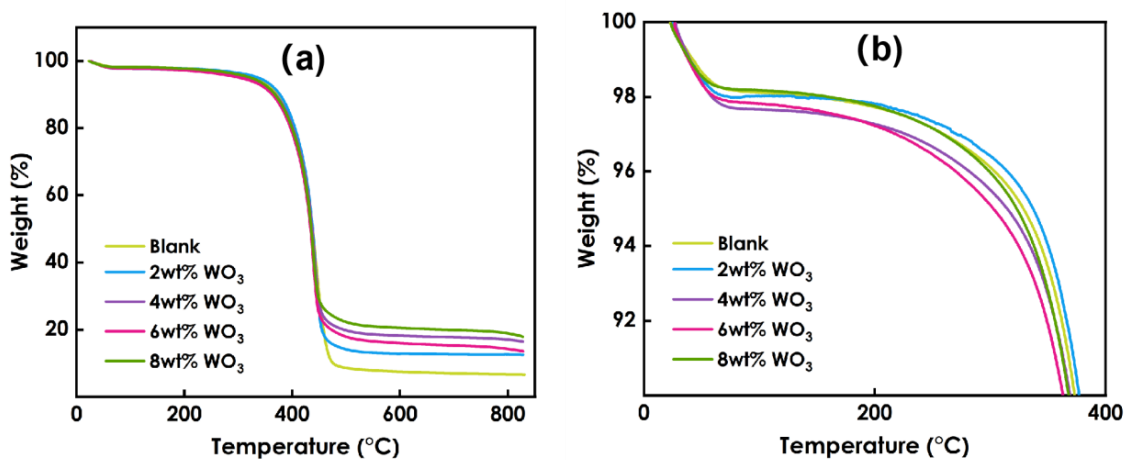

Figure 8. TG data of coatings prepared using different amounts of WO$_3$:(**a**) the temperature between 0 − 800°C, (**b**) the temperature between 0 − 400°C.
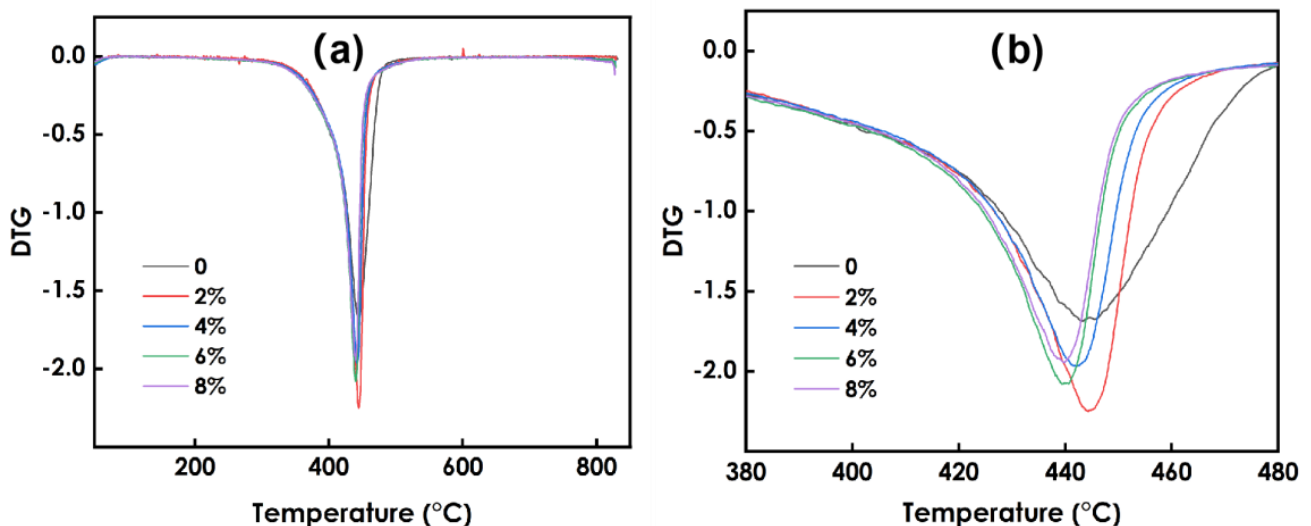

Figure 9. DTG data of coating sprepared using different amounts of WO$_3$: (**a**) the temperature between 0–800°C, (**b**) the temperature between 380–480°C.

3.9. Haze and Mechanical Properties of Composite Coatings

As presented in Table 1, the addition of nanoparticles to the coatings markedly improves the hardness, but negatively affects their adhesion and, with increasing nano-WO₃ content, the haze of the film gradually increases. For 6% WO₃, the hardness of the coating

can reach 2H, the adhesion of the coating can reach 3B, and the haze of the coating is 1.8. Thus, the coating has excellent scratch resistance, excellent adhesion, low haze, and good transparency. When the amount of dispersion is 8%, the hardness of the coating can reach 3H, but the adhesion of the coating is 0B.

Table 1. Coating performance test.

	0	2%	4%	6%	8%
Haze	0.2	0.8	1.2	1.8	2.6
Hardness	HB	2H	2H	2H	3H
Adhesion	5B	5B	4B	3B	0B

3.10. Optical Properties of Cured Coating

In Figure 10, the left and right ordinates represent the visible light transmission rate of the coating and the infrared light blocking rate of the coating, respectively. When no nano-WO_3 is added, the visible light transmittance of the coating is 96%, and the infrared blocking rate is 3%. When 2% nano-WO_3 dispersion is added, the visible light transmittance of the coating is 88%, and the infrared blocking rate is 46%. With the addition of increasing amounts of nano-WO_3 dispersion, the visible light transmittance of the coating film gradually decreases, and the infrared blocking rate gradually increases. When the addition amount is 6%, the visible light transmittance is 70%, the infrared blocking rate is 90%, and the thermal insulation performance of the coating film is excellent. When the addition amount is 8%, the infrared blocking rate is 96%, the visible light transmittance is 62%, and the clarity of the coating film decreases.
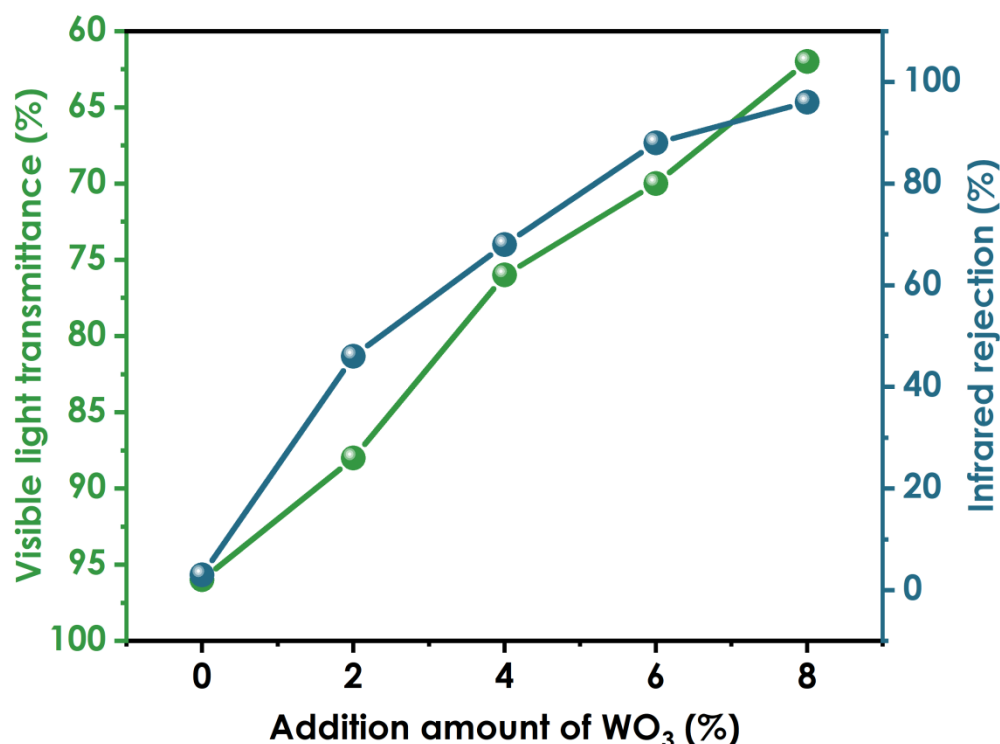

Figure 10. Optical properties of coatings prepared using different amounts of WO_3.

4. Conclusions

In this study, the high-energy ball-milling method was used to grind and disperse nano-WO_3, and the nano-WO_3 was added to an UV—curing system to prepare UV-curable organic–inorganic composite films. The results showed that the organic–inorganic composite UV-curable coating doped with nano-WO_3 had excellent infrared barrier performance,

and excellent mechanical and optical properties. When 6 wt% nano-WO_3 was added, the visible light transmittance of the coating is 70%, the infrared barrier rate is 90%, the hardness of the composite coating is 3H, and the adhesion is 3B. Using high-energy sphere method to modify inorganic particles has many advantages. It can not only significantly reduce the reaction activation energy, but also refine the grains, greatly improve the powder activity, and improve the particle distribution uniformity. Compared with other modification methods, this method is simple and efficient. This product could find potential applications in glass for windows, automobiles, and aircraft.

Author Contributions: Conceptualization, Z.W. and R.Z.; methodology, R.Z.; software, T.L.; validation, Z.W., R.Z. and T.L.; formal analysis, T.C.; investigation, Z.W.; resources, T.L.; data curation, T.L.; writing—original draft Z.W.; writing—review and editing, R.Z.; visualization, Z.W.; supervision, T.L.; project administration, Z.W.; funding acquisition, R.Z. All authors have read and agreed to the published version of the manuscript.

Institutional Review Board Statement: Not applicable.

Informed Consent Statement: Informed consent was obtained from all subjects.

Data Availability Statement: The data presented in this study are available on request from the corresponding author.

Conflicts of Interest: The authors declare no conflict of interest.

References

1. Zhang, H.; Liu, J.; Shi, F.; Jiang, S.; Song, X.; Wasim, M.; Song, X.; Ma, J. Controlling the growth of hexagonal Cs_xWO_3 nanorods by Li^+-doping to further improve its near infrared shielding performance. *Sol. Energy Mater. Sol. Cells* **2022**, *238*, 111612. [CrossRef]
2. Yang, C.; Chen, J.-F.; Zeng, X.; Cheng, D.; Cao, D. Design of the Alkali-Metal-Doped WO_3 as a Near-Infrared Shielding Material for Smart Window. *Ind. Eng. Chem. Res.* **2014**, *53*, 17981–17988. [CrossRef]
3. Lin, C.H.; Lee, G.B.; Lin, Y.H.; Chang, J. A fast prototyping process for fabrication of microfluidic systems on soda-lime glass. *J. Micromech.Microeng.* **2001**, *11*, 726–732. [CrossRef]
4. Mirsayar, M.; Joneidi, V.; Petrescu, R.; Petrescu, F.; Berto, F. Extended MTSN criterion for fracture analysis of soda lime glass. *Eng. Fract. Mech.* **2017**, *178*, 50–59. [CrossRef]
5. Maiorov, V. Light-Transparent Infrared Filters with Dispersed Plasmonic Nanoparticles. *Glass Phys. Chem.* **2020**, *46*, 203–217. [CrossRef]
6. Nair, A.-S.; Keerthana, C.S.; Abraham, J.-E.; Jeorge, P.; Biju, P.R.; Unniklishnan, N.V. Effect of substrate temperature on the near-infrared shielding properties of WO_3-X thin films deposited by RF magnetron sputtering. *Vacuum* **2022**, *202*, 111143. [CrossRef]
7. Alzahran, J.S.; Lebedev, A.V.; Avanesov, S.A.; Hammoud, A.; Alrowaili, Z.A.; Mahmoud, Z.M.M.; Olarinoye, I.O.; Sriwunkum, C.; Al-Buriahi, M.S. Synthesis, optical properties and radiation shielding performance of TeO2-Na2O-BaO-WO3 glass system. *Optiks* **2022**, *261*, 169167. [CrossRef]
8. Nguyen, T.K.N.; Adèle, R.; Maxence, W.; Dumait, N.; Paofai, S.; D Benjamin, D.; Whnagwui, C.; Ohashi, N.; Cordier, S.; Grasset, F. New ultra-violet and near-infrared blocking filters for energy saving applications: Fabrication of tantalum metal atom cluster-based nanocomposite thin films by electrophoretic deposition. *J. Mater. Chem. C Mater. Opt. Electron. Devices* **2017**, *5*, 10477–10484. [CrossRef]
9. Shen, B.; Wang, Y.; Lu, L.; Yang, H. Spraying fabrication of spectrally selective coating with improved near-infrared shielding performance for energy-efficient glazing. *Ceram. Int.* **2021**, *47*, 18991–18997. [CrossRef]
10. Assadullah, I.; Bhat, A.A.; Malik, J.H.; Malik, K.A.; Tomar, R.; Khandy, S.A. Electronic structure, optical, photocatalytic and charge storage performance of WO_3 nanostructures. *J. Phys. Chem. Solids* **2022**, *165*, 110649. [CrossRef]
11. Du, W.-C.; Xie, J.; Xia, L.; Liu, Y.; Zhang, Y. Study of new solar film based on near-infrared shielding. *J. Photochem. Photobiol. A Chem.* **2021**, *418*, 113410. [CrossRef]
12. Jiang, S.; Miao, D.; Xu, J.; Shang, S.; Ning, X.; Zhu, P. Preparation and characterization of shielding textiles to prevent infrared penetration with Ag thin films. *J. Mater. Sci. Mater. Electron.* **2016**, *28*, 3542–3547. [CrossRef]

13. Wang, M.; Xu, Y.; Liu, Y.; Wu, W.; Xu, S. Synthesis of Sb-doped SnO_2 (ATO) hollow microspheres and its application in photo-thermal shielding coating. *Prog. Org. Coat.* **2019**, *136*, 105229. [CrossRef]

14. Zhang, Z.; Zhang, R.; Xu, L.; Li, J.; Yang, L.; Bolshakov, A.; Zhu, J. Visible and infrared optical modulation of PSLC smart films doped with ATO nanoparticles. *Dalton Trans.* **2021**, *50*, 10033–10040. [CrossRef] [PubMed]

15. Wilkins, R.W.T.; Ito, J. Infrared spectra of some synthetic talcs. *Am. Mineral.* **1967**, *52*, 1649–1661.

16. Shen, B.; Wang, Y.; Lin, L.; Yang, H. Synthesis and characterization of Sb-doped SnO_2 with high near-infrared shielding property for energy-efficient windows by a facile dual-titration co-precipitation method. *Ceram. Int.* **2020**, *46*, 18518–18525. [CrossRef]

17. Khan, A.F.; ul Abadeen, Z.; Hanif, M.B.; Saleem, M.S.; Naveed, K.; Bashir, K.; Ahmad, I. Multi-layer MgF_2/ITO coatings for electromagnetic interference shielding. *Mater. Chem. Phys.* **2021**, *272*, 125009. [CrossRef]

18. Chao, L.; Bao, L.; Wei, W.; Tegus, O. A review of recent advances in synthesis, characterization and NIR shielding property of nanocrystalline rare-earth hexaborides and tungsten bronzes. *Sol. Energy* **2019**, *190*, 10–27. [CrossRef]

19. Zeng, X.; Zhou, Y.; Ji, S.; Lou, H.; Yao, H.; Huang, X.; Jin, P. The preparation of a high performance near-infrared shielding Cs_xWO_3/SiO_2 composite resin coating and research on its optical stability under ultraviolet illumination. *J. Mater. Chem. C Mater. Opt. Electron. Devices* **2015**, *3*, 8050–8060. [CrossRef]

20. Gao, H.; Liang, Y.; Li, R.; Huang, H.; Peng, W. Eye-Friendly Reflective Structural Colors with Shortwave Infrared Shielding. *Adv. Opt. Mater.* **2022**, *10*, 2101342. [CrossRef]

21. Gateau, T.; Ayaz, H.; Dehais, F. In silico vs. Over the Clouds: On-the-Fly Mental State Estimation of Aircraft Pilots, Using a Functional Near Infrared Spectroscopy Based Passive-BCI. *Front. Hum. Neurosci.* **2018**, *12*, 187. [CrossRef]

22. Fayad, A.M.; Ouis, M.A.; Batal, F.H.; Eibatal, H.A. Shielding Behavior of Gamma-Irradiated MoO_3 or WO_3-Doped Lead Phosphate Glasses Assessed by Optical and FT Infrared Absorption Spectral Measurements. *Silicon* **2017**, *10*, 1873–1879. [CrossRef]

23. Ren, Y.; Zhou, X.; Wang, Q.; Zhao, Y. Combined redox and plasmonic electrochromic effects in WO_3/ITO double-layer films. *J. Sol-Gel Sci. Technol.* **2018**, *85*, 732–742. [CrossRef]

24. Guo, C.; Yin, S.; Zhang, P.; Yan, M.; Adachi, K.; Chonan, T.; Sato, T. Novel synthesis of homogenous Cs_xWO_3 nanorods with excellent NIR shielding properties by a water controlled-release solvothermal process. *J. Mater. Chem.* **2010**, *20*, 8227–8229. [CrossRef]

25. Li, C.; Kang, C.; Huang, S.; Lee, P.; Kuo, H.; Hsu, F. Near infrared radiation shielding using CsxWO3 nanoparticles for infrared mini light-emitting diodes. *Mater. Lett.* **2020**, *260*, 126961. [CrossRef]

26. Zali, V.S.; Jahanbakhsh, O.; Ahadzadeh, I. Preparation and evaluation of gamma shielding properties of silicon-based composites doped with WO_3 micro- and nanoparticles. *Radia. Phy. Chem.* **2022**, *197*, 110–152. [CrossRef]

27. Zhou, Y.; Huang, A.; Zhou, H.; Ji, S.; Jin, P. Organic-Inorganic hybrid optical foils with strong visible reflection, excellent near infrared-shielding ability and high transparency. *Nanotechnology* **2018**, *29*, 95705. [CrossRef]

28. Fernandes, G.E.; Lee, D.; Kim, J.; Kim, K.; Xu, J. Infrared and microwave shielding of transparent Al-doped ZnO superlattice grown via atomic layer deposition. *J. Mater. Sci.* **2013**, *48*, 2536–2542. [CrossRef]

29. Li, T.; Liu, J.; Shi, F.; Song, X.; Zhang, H.; Zhang, H.; Ma, C.; Zhu, K.; Liu, Y. Construction of a novel highly porous $BiOBr$/Cs_xWO_3@SiO_2 composite aerogel: Adsorption/self-heating photocatalytic synergistic degradation of antibiotics and mechanism study. *J. Environ. Chem. Eng.* **2022**, *10*, 107785. [CrossRef]

30. Liu, J.; Ran, S.; Fan, C.; Qiao, Y.; Shi, F.; Yang, J.; Chen, B.; Liu, S. One pot synthesis of Pt-doped Cs_xWO_3 with improved near infrared shielding for energy-saving film applications. *Sol. Energy* **2019**, *178*, 17–24. [CrossRef]

31. Song, X.; Liu, J.; Shi, F.; Fan, C.; Ran, S.; Zhang, H.; Zou, Z. Facile fabrication of $K_mCs_nWO_3$ with greatly improved near-infrared shielding efficiency based on W^{5+}-induced small polaron and local surface plasmon resonance (LSPR) modulation. *Sol. Energy Mater. Sol. Cells* **2020**, *218*, 110769. [CrossRef]

32. Ghamdi, H.A.; Elsafi, M.; Sayyed, M.I.; Almuqrin, A.H.; Tamayo, P. Performance of newly developed concretesincorporating WO_3 and barite as radiation shielding material. *JMR T* **2022**, *19*, 4103–4114.

33. Li, X.; Zhu, L.; Peng, H.; Chen, L.; Liu, X. Synthesis of organic and inorganic hybrid nanoparticles as multifunctional photoinitiator and its application in UV-curable epoxy acrylate-based coating systems. *Prog. Org. Coat.* **2020**, *141*, 105565. [CrossRef]

34. Nguyen, T.V.; Dao, P.; Duong, K.; Le, T.; Dao, P.; Duong, H.; Mac, V.P.; Nguyen, A.M. Effect of R-TiO_2 and ZnO nanoparticles on the UV-shielding efficiency of water-borne acrylic coating. *Prog. Org. Coat.* **2017**, *110*, 114–121. [CrossRef]

35. Wang, C.; Zhang, J.; Chen, J.; Shi, J.; Zhao, Y.; He, M.; Ding, L. Bio-Polyols based waterborne polyurethane coatings reinforced with chitosan-modified ZnO nanoparticles. *Int. J. Biol. Macromol.* **2022**, *208*, 97–104. [CrossRef]

36. Dao, P.; Nguyen, T.D.; Nguyen, T.C.; Nguyen, A.H.; Mac, V.P.; Tran, H.T.; Phung, T.L.; Vu, Q.T.; Vu, D.H.; Ngo, T.C. Assessment of some characteristics, properties of a novel waterborne acrylic coating incorporated TiO_2 nanoparticles modified with silane coupling agent and Ag/Zn zeolite. *Prog. Org. Coat.* **2022**, *163*, 106641. [CrossRef]

37. Habib, S.; Amani, H.; Ramazan, K.; Ahmed, E.M.; Shakoor, R.A. Self-Healing behavior of epoxy-based double-layer nanocomposite coatings modified with Zirconia nanoparticles. *Mater. Des.* **2021**, *207*, 109839. [CrossRef]